

Article

Dynamic and Thermal Investigations of the Forward Dry-Friction Whirl/Whip of a Vertical Rotor-AMB System during Touchdowns

Zilin Li ¹, Mindong Lyu ², Guojun Yang ³, Jingjing Zhao ³, Yuming Wang ¹ and Zixi Wang ^{1,*}¹ State Key Laboratory of Tribology, Tsinghua University, Beijing 100084, China² Institute of Magnetic Levitation and Electromagnetic Propulsion, China Aerospace Science & Industry Corp., Beijing 100143, China³ Institute of Nuclear and New Energy Technology, Tsinghua University, Beijing 100084, China

* Correspondence: zxwang@tsinghua.edu.cn; Tel.: +86-13521026173

Abstract: When an active magnetic bearing (AMB) rotor drops, it impacts the touchdown bearing (TDB) and produces friction on its surface. The vertical AMB rotor has no stable support in the radial direction, and the rotor exhibits a violent whirl motion in the gap of the TDB. In this study, a complete dynamic and thermal model of the AMB-rotor-TDB system was established, and the complete drop process was simulated. When the rotor dropped, it obtained stable support after several bounces on the thrust surface of the TDB inner ring in the axial direction. In the radial direction, the rotor entered whirl motion after the initial collisions. There is a natural whirl frequency so that the drop forward whirl is divided into the dry-friction whirl and whip states. The contact force and heat generation of the TDB were monitored in the simulation and had different performances in the two states. Both the initial collisions and the stabilized whirl motions were studied to evaluate the reliability of the TDB. Finally, a series of drop tests were performed, and the experimental results were in good agreement with the simulation.

Keywords: active magnetic bearing; touchdown bearing; rotor dynamics; dry-friction whirl/whip



Citation: Li, Z.; Lyu, M.; Yang, G.; Zhao, J.; Wang, Y.; Wang, Z. Dynamic and Thermal Investigations of the Forward Dry-Friction Whirl/Whip of a Vertical Rotor-AMB System during Touchdowns. *Actuators* **2022**, *11*, 291. <https://doi.org/10.3390/act11100291>

Academic Editor: Takeshi Mizuno

Received: 14 September 2022

Accepted: 10 October 2022

Published: 11 October 2022

Publisher's Note: MDPI stays neutral with regard to jurisdictional claims in published maps and institutional affiliations.



Copyright: © 2022 by the authors. Licensee MDPI, Basel, Switzerland. This article is an open access article distributed under the terms and conditions of the Creative Commons Attribution (CC BY) license (<https://creativecommons.org/licenses/by/4.0/>).

1. Introduction

When an active magnetic bearing (AMB) rotor drops to touchdown bearing (TDB), the rotor cannot get stable support. Therefore, the TDB will be subject to violent collisions, friction, and heat generation, which can cause failure and damage to the TDB in severe cases [1]. Although the drop dynamic response at the initial stage is highly complex, the international standard ISO14839-4 [2] characterizes the rotor drop dynamic response to evaluate the impact and friction forces on the TDB to determine its reliability. Lyu [3,4] proposed a drop trajectory identification method based on the instantaneous frequency transient response. The online condition monitoring implemented in the system was mainly used for vibration suppression and rotor re-suspension [5]. Some external means, such as the installation of squeeze film dampers between the TDB and the bearing support in a study by Kang [6], can also effectively suppress the transient rotor drop vibration response.

Ishii [7] performed early research on the transient response of the AMB-rotor drop process and established an analytical model of the Jeffcott rotor and TDB to study the influence of nonlinear contact on the transient vibration of the bearing. Kärkkäinen [8] established a flexible rotor model based on Timoshenko theory and a TDB model based on a detailed ball bearing model. The Hunt-Crossley contact model [9], which evaluates the collision between the rotor and the TDB, was also widely used in subsequent drop studies. Studies have shown that the dynamic response of rotor drop is affected by many factors, such as the stiffness damping coefficient [10], friction coefficient [11], rotor unbalance [12], and rotor installation misalignment [13]. In addition to the drop dynamic responses of the

rotor and the TDB, the heat generation and temperature rise of the TDB are other important monitoring parameters when studying the reliability of the system. The maximum contact force generally occurs in the initial impact of the drop, and the temperature increases continuously with the friction torque as the drop decelerates. Gupta [14] established a dynamic, thermal-coupled model of rolling bearings. The heat in the bearing is mainly caused by internal frictional resistance; note that hybrid ceramic ball bearings generate less heat than steel ball bearings. For the drop process, the friction between the rotor and the inner ring contact surface also needs to be considered in the thermal model. Sun [15] established an effective thermal model of the drop process, including a one-dimensional radial heat transfer grid, and found that the thermal growth at the rotor–TDB interface is the highest, indicating that the contact friction heating power between the rotor and the TDB is higher than that in the TDB.

Most of the above studies and models are based on horizontally oriented rotors, but there are some vertically oriented rotors in industrial applications [16,17]. There is no difference between the two rotor types in the control level of AMB. However, in a drop study, the direction of gravity greatly affected the dynamic response. Hawkins [18] conducted a drop test of a vertical rotor, and it took 2.7 h for the rotor to decelerate from 36,000 r/min to a complete stop with an unassisted spin down from its full speed. Since the rotor is radially unconstrained, friction in the thrust surface brings more constant wear and heating. Although Zhao [19] modeled and simulated the drop dynamics and thermal behaviors of the vertical rotor, the frictional heat generation of the contact surface in the thrust surface was not considered in the model.

In addition, some of our experiments (Figure 1) show that TDB damage does not occur at the drop moment; instead, the TDB is damaged by the exposure to high temperatures during the drop period. Therefore, it is necessary to monitor the entire drop process, especially regarding temperature and stress evaluations. At present, the research in the field mainly focuses on the contact force and temperature changes in the drop transient response, and there are few accurate simulation studies on the full drop process. In this paper, the corresponding thermal model is established based on Wilkes's research [20,21] on the dynamic response of the vertical rotor dry-friction whirl/dry-friction whip. The whole drop process is simulated and analyzed, particularly the thermal growth difference between the rolling friction of the rotor–TDB dry-friction whirl and the sliding friction of the rotor–TDB dry-friction whip. The simulation results are verified by experiments.

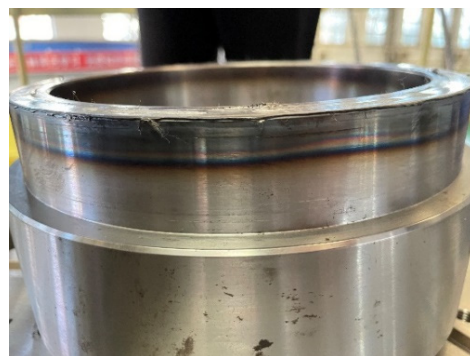


Figure 1. Burn and wear scars on the sleeve after severe TDB failure.

2. Modeling

2.1. Friction between the Rotor and TDB

The types of contact in the system need to be defined before establishing a dynamic model. There are three types of contact between the rotor and TDB: axial surface contact, radial line contact, and internal bearing contact. The frictional forces for all three types of contact are calculated by the Coulomb friction model. For the first two forms of contact,

the Hunt–Crossley collision contact model [9] is used, which can accurately describe the collision contact force and puncture depth [22]:

$$F_r(t) = Kx^\beta(t) \left(1 + \frac{3}{2} \lambda \dot{x}(t) \right) \quad \text{when } x(t) > 0 \tag{1}$$

The contact stiffness is given by the Hertz contact model:

$$K = \frac{4}{3 \left(\frac{1-\nu_1^2}{E_1} + \frac{1-\nu_2^2}{E_2} \right)} \left(\frac{r_1 r_2}{r_1 + r_2} \right)^{\frac{1}{2}} \tag{2}$$

Among the first two contact types, the collision friction calculation for the axial contact surface is more complicated (Figure 2). To calculate the collision friction on the entire surface, the relative motion state of the rotor and inner ring of the TDB must be solved. First, the friction for the contact point A is calculated as follows:

$$v_{A,rb} \vec{v}(r, \varphi) = \left[\dot{\rho} + (\dot{\theta}_r - \dot{\theta}_b) r \sin \varphi \right] \vec{i} + \left[(\dot{\alpha} - \dot{\theta}_r) \rho - (\dot{\theta}_r - \dot{\theta}_b) r \cos \varphi \right] \vec{j} \tag{3}$$

Then, the friction force and friction torque are calculated by integrating the whole surface as follows:

$$F_{a,i} = -P_a \mu_a \cdot \int_{R_1}^{R_2} \int_0^{2\pi} \frac{\left[\dot{\rho} + (\dot{\theta}_r - \dot{\theta}_b) r \sin \varphi \right] \vec{i} \cdot r d\varphi dr}{\left\{ \left[\dot{\rho} + (\dot{\theta}_r - \dot{\theta}_b) r \sin \varphi \right]^2 + \left[(\dot{\alpha} - \dot{\theta}_r) \rho - (\dot{\theta}_r - \dot{\theta}_b) r \cos \varphi \right]^2 \right\}^{\frac{1}{2}}} \tag{4}$$

$$F_{a,j} = -P_a \mu_a \cdot \int_{R_1}^{R_2} \int_0^{2\pi} \frac{\left[(\dot{\alpha} - \dot{\theta}_r) \rho - (\dot{\theta}_r - \dot{\theta}_b) r \cos \varphi \right] \vec{j} \cdot r d\varphi dr}{\left\{ \left[\dot{\rho} + (\dot{\theta}_r - \dot{\theta}_b) r \sin \varphi \right]^2 + \left[(\dot{\alpha} - \dot{\theta}_r) \rho - (\dot{\theta}_r - \dot{\theta}_b) r \cos \varphi \right]^2 \right\}^{\frac{1}{2}}} \tag{5}$$

$$M_a = \frac{2F_a \mu_a (R_2^3 - R_1^3)}{3(R_2^2 - R_1^2)} \tag{6}$$

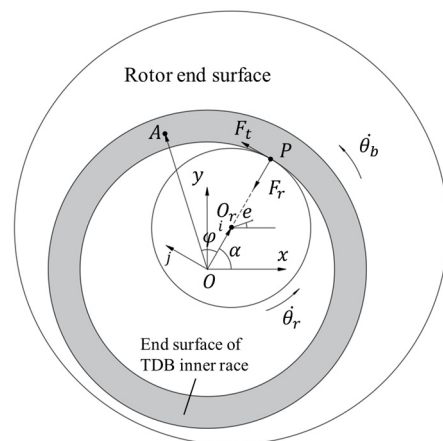


Figure 2. Contact model of the rotor and TDB inner ring.

2.2. Dynamics of the Vertical Rotor–TDB System

TDBs can be described by some classical models of rolling bearings [23]. Since it is difficult to design a lubrication system, the TDB is usually in the state of no lubrication or grease lubrication, so the most important thing that needs clarification is the friction torque

inside the bearing, which is directly related to the energy loss and temperature rise of the TDB. A high bearing temperature can lead to lubricant deterioration, wear increase, and even bearing damage.

The internal friction torque of the bearing is calculated by Palmgren’s empirical formula [24]:

$$M_b = M_0 + M_1 \tag{7}$$

$$M_0 = \begin{cases} 160 \times 10^{-7} f_0 d_m^3, & v\dot{\theta}_b \leq 2000 \\ f_0 (v\dot{\theta}_b)^{\frac{2}{3}} d_m^3 \times 10^{-7}, & v\dot{\theta}_b > 2000 \end{cases} \tag{8}$$

$$M_1 = f_1 P_1 d_m \tag{9}$$

where M_0 represents the friction torque related to the bearing type, the bearing rotational speed, and the lubricant properties, $N \cdot mm$. M_1 represents the friction and wear related to elastic hysteresis and local differential sliding, $N \cdot mm$.

In addition, there is a spin friction torque that affects the heat generation of the bearing at high speeds, which is calculated for the inner and outer ring and each rolling body as follows:

$$M_{si} = \frac{3}{8} \mu_i F_i a_i L_i(k) ; M_{so} = \frac{3}{8} \mu_o F_o a_o L_o(k) \tag{10}$$

$$M_{ij} = \frac{d_b}{z \cdot d_i} M ; M_{oj} = \frac{d_b}{z \cdot d_o} M \tag{11}$$

By considering the vertical magnetic bearing rotor as the modeling object, the rigid rotor dynamics model is established in Figure 3. According to the Lagrange equation, the dynamic equation of the rotor falling in three directions is established as follows:

$$\begin{cases} m_r \left[\ddot{x}_r - e \sin(\theta_r) \ddot{\theta}_r - e \cos(\theta_r) \dot{\theta}_r^2 \right] = -(F_r - F_{a,i}) \cos \alpha - (F_t + F_{a,j}) \sin \alpha \\ m_r \left[\ddot{y}_r + e \cos(\theta_r) \ddot{\theta}_r - e \sin(\theta_r) \dot{\theta}_r^2 \right] = -(F_r - F_{a,i}) \sin \alpha + (F_t + F_{a,j}) \cos \alpha \\ m_r \ddot{z} = -m_r g + F_{a,z} \\ m_r e \left[-\sin(\theta_r) \ddot{x}_r + \cos(\theta_r) \ddot{y}_r \right] + (m_r e^2 + J_r) \ddot{\theta}_r = F_r e \sin(\alpha - \theta_r) + F_t (r - e \cos(\alpha - \theta_r)) - M_a \end{cases} \tag{12}$$

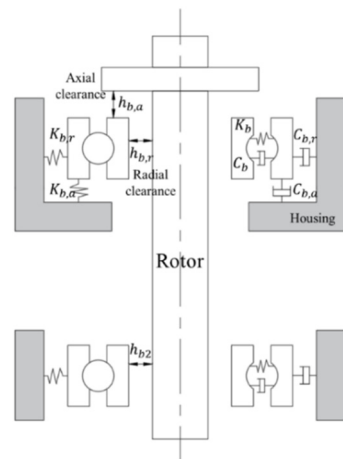


Figure 3. Contact model of the rotor and TDB inner ring.

The dynamic equation of the TDB inner ring can be written as follows:

$$M_b \ddot{x} = F_c \tag{13}$$

where $M_b = [m_b \ m_b \ J_b]$ and $x = [x_b \ y_b \ \theta_b]^T$, which are the mass and displacement matrices of the TDB inner ring, respectively. F_c represents the contact force and friction matrix on the TDB inner ring, and it is defined as follows:

$$F_c = \begin{bmatrix} (F_r - F_{a,i}) \cos \alpha + (F_t + F_{a,j}) \sin \alpha - F_{nb} \cos \alpha_b + (M/r_s) \sin \alpha_b \\ (F_r - F_{a,i}) \sin \alpha - (F_t + F_{a,j}) \cos \alpha - F_{nb} \sin \alpha_b - (M/r_s) \cos \alpha_b \\ -F_t r_i - M_b + M_a \end{bmatrix} \quad (14)$$

2.3. Thermal Model of the Rotor–TDB System

During rotor drop, heat is generated by the frictional forces between the rotor and the TDB inner ring and by the frictional torque inside the TDB. This heat causes a temperature rise in the bearing, which in turn changes the bearing dynamics and performance. Therefore, the thermal characterization of the drop is also a crucial aspect of the rotor–TDB system reliability assessment.

The heat generation mainly comes from the contact friction defined in the previous section on dynamics. The node heat exchanges comprise the heat conduction and convection of each component and the air, respectively. The temperature node model and the heat transfer grid model are established as shown in Figure 4. The heat transfer capability of each part is determined by the contact thermal resistance. The contact thermal resistance of each part is calculated as follows:

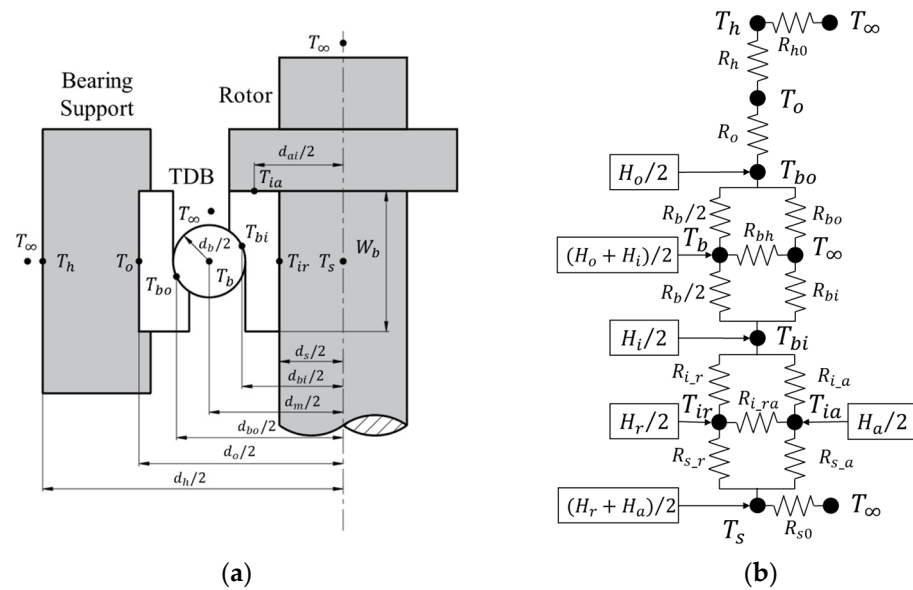


Figure 4. Thermal model of the rotor–TDB system: (a) Temperature node model; (b) Heat transfer grid model.

Rolling element:

$$R_b = \frac{2z}{k_b \pi d_b}; \quad R_{bh} = \frac{z}{h_b \pi d_b^2} \quad (15)$$

TDB inner ring:

$$R_{bi} = \frac{z}{h_i \pi d_{bi} W_b}; \quad R_{i,r} = \frac{\ln(d_{bi}/d_s)}{2k_i \pi W_b}; \quad R_{i,a} = \frac{2W_b}{k_i \pi (d_{bi}^2 - d_s^2)}; \quad R_{i,ra} = \frac{2}{k_i \pi \sqrt{(d_{ai} - d_s)^2 + W_b^2}} \quad (16)$$

TDB outer ring:

$$R_{bo} = \frac{z}{h_o \pi d_{bo} W_b}; \quad R_o = \frac{\ln(d_o/d_{bo})}{2k_o \pi W_b} \quad (17)$$

Rotor:

$$R_{s_r} = \frac{1}{k_s \pi W_b}; R_{s_a} = \frac{2}{k_s \pi d_{ai}}; R_{s0} = \frac{4L_s}{k_s \pi d_s^2} + \frac{4}{h_s \pi d_s^2} \quad (18)$$

TDB support:

$$R_h = \frac{\ln(d_h/d_o)}{2k_h \pi W}; R_{h0} = \frac{1}{h_h \pi d_h W} \quad (19)$$

Assuming that the heat flux is uniformly distributed radially, the heat transfer mesh of the system can be established, and the temperature of each node can be solved with a first-order differential equation:

$$mC_p \Delta T = \Delta Q \quad (20)$$

Overall, the calculation process can be summarized by Figure 5. The axial dynamic response, radial dynamic response, and thermal response of the system are calculated in sequence. Among them, the spatial position relationship of the rotor and the TDB causes the axial and radial dynamics to influence each other. The temperature change caused by the dynamics also affects the dynamic response because of the viscosity–temperature characteristics of the lubricant.

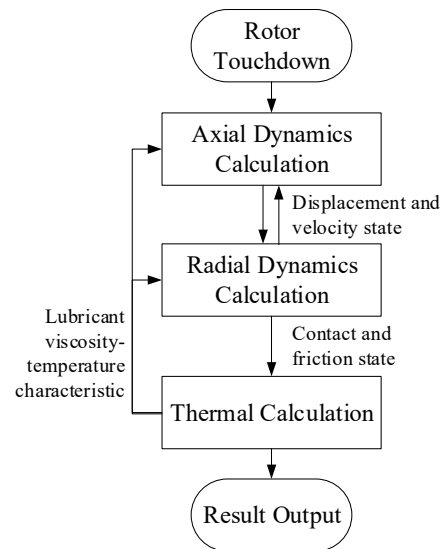


Figure 5. Contact model of the rotor and TDB inner ring.

3. Rotor Touchdown Experiments

To verify the validity of the model, an AMB–rotor–TDB system experimental bench with a rigid rotor is built, which is capable of horizontal and vertical arrangements and is suitable for various research needs. The mechanical structure is modularized, relying on four optical axes to ensure coaxial positioning accuracy. It mainly consists of the rotor, high-speed asynchronous motor, radial AMB, axial AMB, and TDBs (see Figure 6). Two sets of TDBs support the rotor; each set of TDB uses a pair of angular contact ball bearings with face-to-face preloaded. The upper TDB bears both axial and radial loads, while the lower TDB only bears radial loads. The axial and radial clearances between the rotor and the TDB are both 0.2 mm. The electrical control section mainly consists of eddy current displacement sensors, a photoelectric speed sensor, analog filter, controller, and power amplifier. The monitoring part consists of a CAN (Controller Area Network) communication card, acquisition card, thermal imager, and host computer, which can record and display key information, such as the rotor trajectory, rotational speed, control current, and PID control parameters. At present, this system has achieved a maximum speed of 36,000 r/min in suspension tests. The relevant parameters of the experimental bench are shown in Table 1.

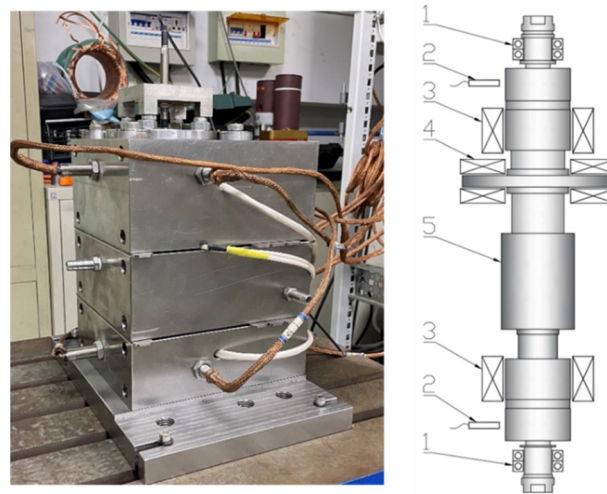


Figure 6. AMB–rotor–TDB drop test bench: 1—TDBs, 2—eddy current sensors, 3—radial AMBs, 4—axial AMB, 5—rotor.

Table 1. Parameters of the AMB–rotor–TDB system.

Parameters	Value
Rotor mass	2.5 kg
Rotor length	293 mm
Rotor moment of inertia	$8957.32 \times 10^{-6} \text{ kg}\cdot\text{m}^2$
Imbalance eccentricity	$1.5 \times 10^{-5} \text{ m}$
Radial magnetic bearings distance	155 mm
Two TDBs' distance	253 mm
Radial AMB clearance	0.3 mm
Axial AMB clearance	0.4 mm
TDB clearance	0.2 mm
Contact friction coefficient	0.12
Motor power	4 kW
Bias current	2 A
Radial AMB current stiffness	81.268 N/A
Radial AMB displacement stiffness	$-5.864 \times 10^5 \text{ N/m}$
Axial AMB current stiffness	50.26 N/A
Axial AMB displacement stiffness	$-2.720 \times 10^5 \text{ N/m}$
Maximum speed	36,000 r/min

The test protocol is as follows: start the AMB to levitate the rotor when the rotor is stationary; use the motor to accelerate the rotor to the set speed; turn off the motor and AMB simultaneously to let the rotor drop freely without applying additional braking force; use the eddy current sensor and photoelectric speed sensor to monitor the rotor trajectory and rotational speed; and use the thermal imager to monitor the temperature change of TDB.

4. Result and Discussion

4.1. Simulation Results

A drop simulation model was performed using the method described in Section 2. The parameters of the experimental bench were substituted into the simulation model calculations. Three cases of rotor drop speed—5000, 10,000, and 20,000 r/min—were used for analysis. The drop trajectory, rotational speed, contact force, and temperature variation were solved for each drop case. The simulations not only focused on the dynamic and thermal responses of the rotor and TDB at the beginning of the drop but also on the entire drop process as the rotor decelerated to its stop.

The simulation results of the rotor dropping to the TDB at 5000 r/min are shown in Figure 7. From the drop trajectory in Figure 7a,b, the rotor initially experienced several collisions before achieving axial stable support. Radially, it entered stable whirl motion, of which the direction was obtained from the rotor speed in Figure 7c,d. Figure 7c,d displays the rotor speed, TDB inner ring speed, and rotor whirl motion. The inner ring accelerated to a speed equal to the rotor soon after the drop, while the whirl speed was initially negative (backward whirl) and then gradually became a forward whirl. Then, the whirl speed increased to the same speed as the rotor, and the two synchronously decelerated to zero velocity. From the force diagram in Figure 7e,f, the maximum contact force occurred in the first few collisions. The maximum axial contact force was 542 N, and the radial maximum contact force was 322 N. According to the temperature change in Figure 7g,h, the most obvious heat generation was in the rolling elements with the fastest heat dissipation. The highest temperature, which was 2.4 °C higher than the ambient temperature, appeared within the first 3 s of the drop.

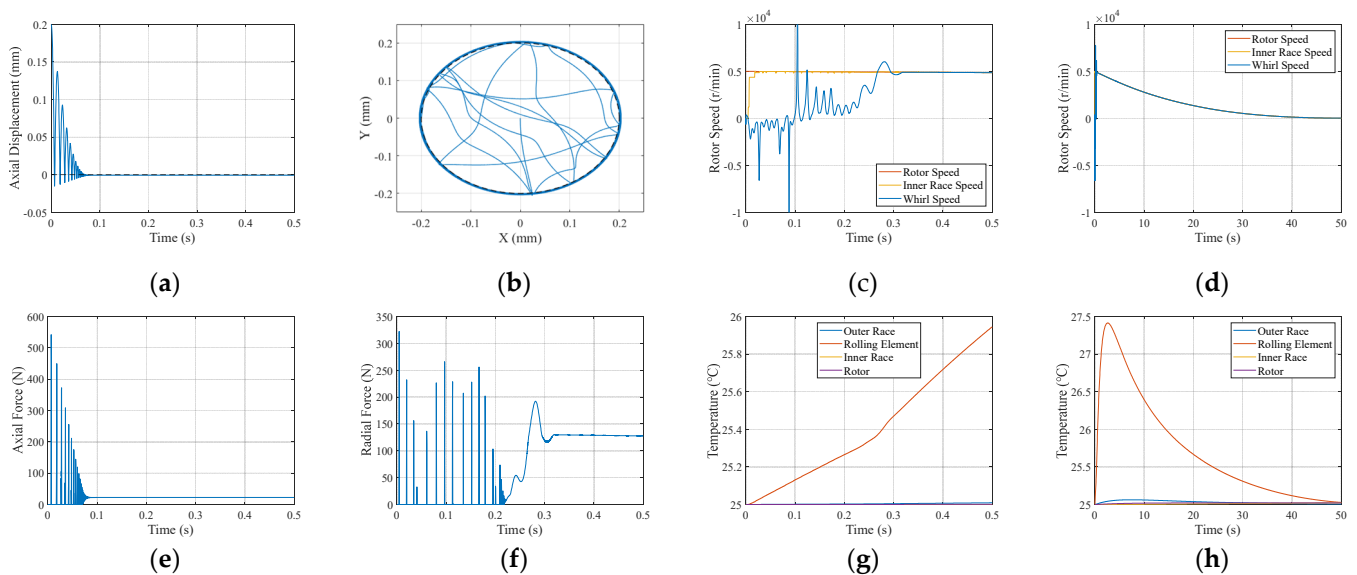


Figure 7. Numerical simulation results of the rotor touchdown at 5000 r/min: (a) Axial displacement, (b) Radial trajectory, (c) Rotor speed change in the first 0.5 s, (d) Rotor speed change for the whole process, (e) Axial contact force of the TDB, (f) Radial contact force of the TDB, (g) Temperature change in the first 0.5 s, (h) Temperature change for the whole process.

The results of increasing the drop speed to 10,000 r/min are shown in Figure 8. The difference of the drop trajectory in Figure 8a,b was not obvious. The most obvious change was in the whirl speed in Figure 8c,d, where the whirl speed could not reach the rotor speed after acceleration; however, the sub-synchronous forward whirl occurred at a fixed speed range (4480–8000 r/min with an average of 6240 r/min) until the rotor decelerated to the whirl speed, and then the rotor and TDB inner ring transitioned to a synchronous whirl and then decelerated to zero velocity. The contact force and temperature rise of the rotor significantly increased as there was an increase in both factors during the transition from sub-synchronous whirl to synchronous whirl. The radial maximum contact force was 716 N. The maximum temperature rise of the rolling element was 9.2 °C.

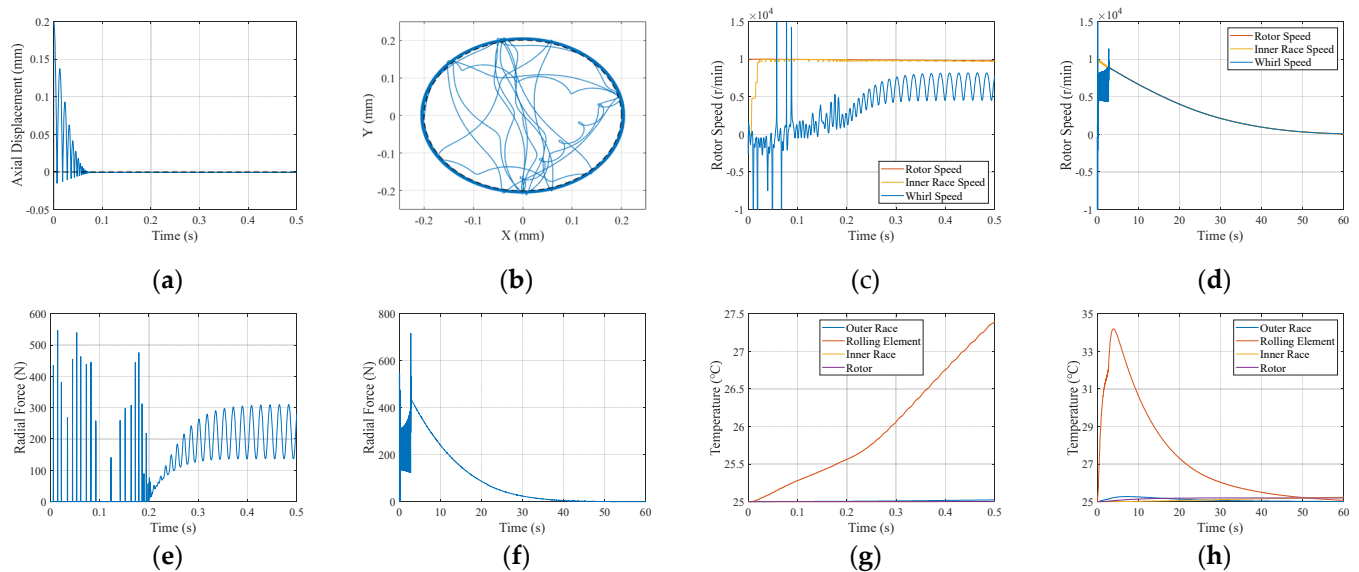


Figure 8. Numerical simulation results of the rotor touchdown at 10,000 r/min: (a) Axial displacement, (b) Radial trajectory, (c) Rotor speed change in the first 0.5 s, (d) Rotor speed change for the whole process, (e) Radial contact force of the TDB in first 0.5 s, (f) Radial contact force of the TDB for the whole process, (g) Temperature change in first 0.5 s, (h) Temperature change for the whole process.

The speed was further increased to 20,000 rpm, and the simulation results are shown in Figure 9. The change in whirl speed showed that the whirl speed remained at 6240 r/min and did not increase with increasing rotor speed, unlike when the speed was 10,000 rpm. In addition, the contact force and heat generation level at the beginning of the drop further increased as the rotor speed increased. The radial maximum contact force was 1155 N. The maximum temperature rise of the rolling element was 10.5 °C. After entering the stable forward whirl motion, the contact force and heat generation did not change much compared to the lower speed, where the contact force was approximately 200 N.

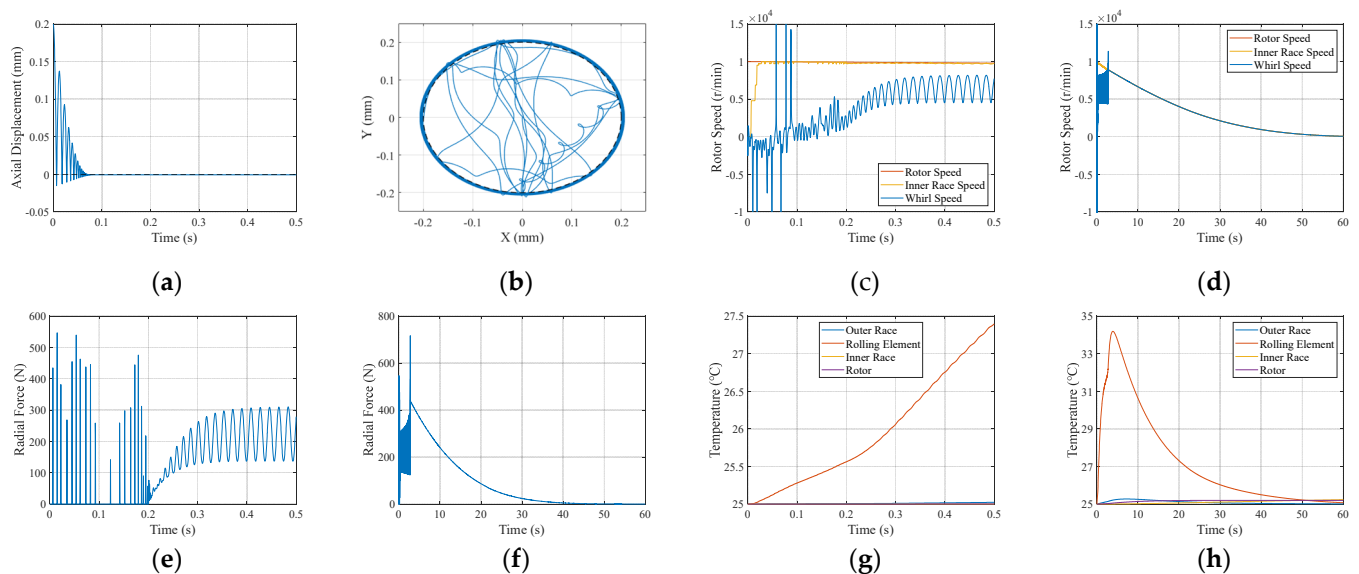


Figure 9. Numerical simulation results of the rotor touchdown at 5000 r/min: (a) Axial displacement, (b) Radial trajectory, (c) Rotor speed change in the first 0.5 s, (d) Rotor speed change for the whole process, (e) Radial contact force of the TDB in the first 0.5 s, (f) Radial contact force of the TDB for the whole process, (g) Temperature change in the first 0.5 s, (h) Temperature change for the whole process.

4.2. Model Analysis

The axial ring surface and tangential contact friction drive the rotor to whirl. The whirl direction depends on the direction of the friction force F_t . In the early stages of the drop, the inner ring is stationary or operating at a low speed, and the F_t direction is opposite to the rotor rotation direction, so the rotor exhibits a backward whirl. After the axial surface causes the inner ring to accelerate, the inner ring will maintain the same speed as the rotor. The total friction direction is the same as the rotor rotation direction, so the rotor will begin to forward whirl after stabilization.

Although the initial collision process is unpredictable, the stable forward whirl state had a certain regularity, which is consistent with the dry-friction whirl and dry-friction whip states expressed by Wilkes [20,21]. These states are defined as follows.

1. **Dry-friction whirl (Dry whirl):** the rotor rolls on the surface of the stator without slipping, and the precession frequency is governed by the radius-to-clearance ratio at the contact location;
2. **Dry-friction whip (Dry whip):** the rotor slides continuously on the surface of the stator, and the precession frequency is controlled by the combined natural frequency of the rotor–stator system.

In the dry-friction whirl state, since the diameters of the rotor and the TDB inner ring are approximately equal, the speeds of the rotor and inner ring are also approximately equal. However, the natural whirl frequency under dry-friction whip is not equal to the natural frequency of the rotor at stable-support [16], which is derived and analyzed below.

It is assumed that after entering a stable forward whirl state, the rotor performs whirl motion with a fixed radius, and the model does not consider the change in the rotational speed that occurs over a short time. Therefore, Equation (12) is simplified and expressed in polar coordinates as follows:

$$m_r \left[\rho_0 \ddot{\alpha} e^{i\alpha} + \rho_0 \dot{\alpha}^2 e^{i\alpha} + e_0 \Omega^2 e^{i\Omega t} \right] = K \rho_0 e^{i\alpha} + (\mu K \rho_0 + F_{a,j}) i e^{i\alpha} \quad (21)$$

Equation (21) is a second-order differential equation for the angular displacement, so there is a special solution of this equation—the natural whirl frequency. In addition, there is a time-dependent imbalance parameter $e_0 \Omega^2 e^{i\Omega t}$, which explains why the simulated natural whirl frequency is not a fixed value but fluctuates within a certain range.

According to the above analysis, the stable whirl speed at each speed level was solved by simulation, and the variation spectrum of whirl speed with the initial drop speed is shown in Figure 10. The switching between the two states of dry-friction whirl and dry-friction whip was distinguished by an obvious critical speed, which was jointly determined by the natural whirl frequency and its fluctuation range.

The two stable forward whirl states were also different in force and heat generation. The dry-friction whirl occurred at a lower speed than the dry-friction whip; therefore, the dry-friction whirl had a lower collision contact force at the beginning of the drop. After entering the dry-friction whip state, the contact force did not continue to rise with increasing drop speed. In the dry-friction whirl state, the rotor rotated synchronously with the TDB inner ring, and there was almost no sliding friction between them. Therefore, the overall heat generation was low, mainly from the internal heat of the bearing. After entering the dry-friction whip state, the sliding friction between the rotor and the inner ring of the TDB became the dominant factor in the heat generation of TDB, so the heat generation was significantly increased compared that of the dry-friction whirl state. With the energy release and deceleration of the rotor, the high-speed rotor also changed from the dry-friction whip state to the dry-friction whirl state when it decelerated to zero velocity. The force and temperature simulation of the entire process helped to accurately assess the reliability of the TDB.

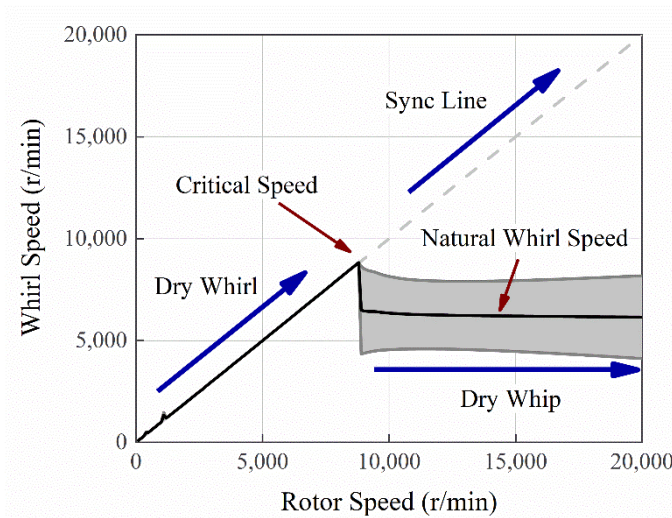


Figure 10. Whirl speed variation spectrum with initial touchdown speed.

4.3. Experimental Verification

After arrangement of the experimental table vertically, a series of drop tests were conducted by setting the rotational speed to 5000 rpm and 20,000 rpm, and the results were obtained, as shown in Figures 11–13. Figure 11 shows the rotor drop trajectory and temperature measured in the experiment, and similar results were obtained at different speed settings.

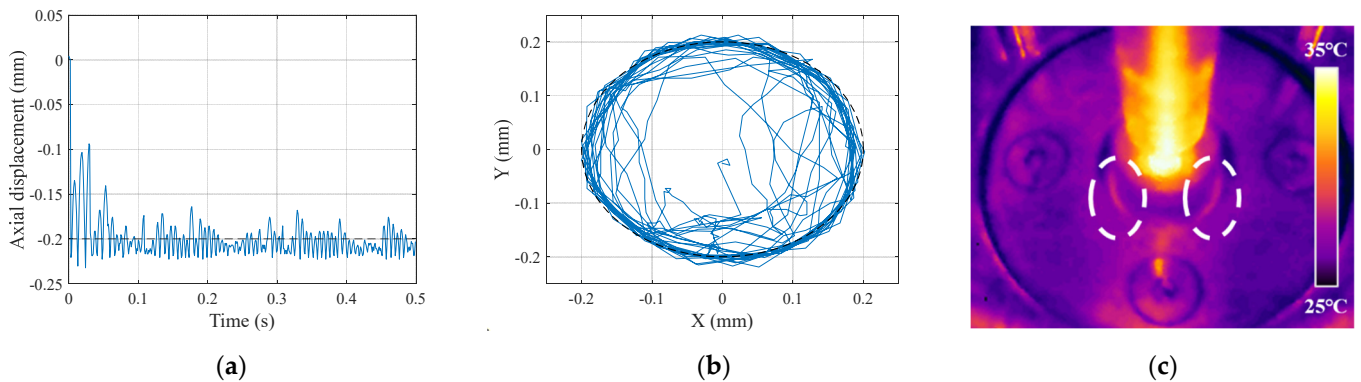


Figure 11. Experimentally measured rotor drop process: (a) Axial displacement, (b) Radial trajectory, and (c) Temperature change (The circle shows the position of TDB).

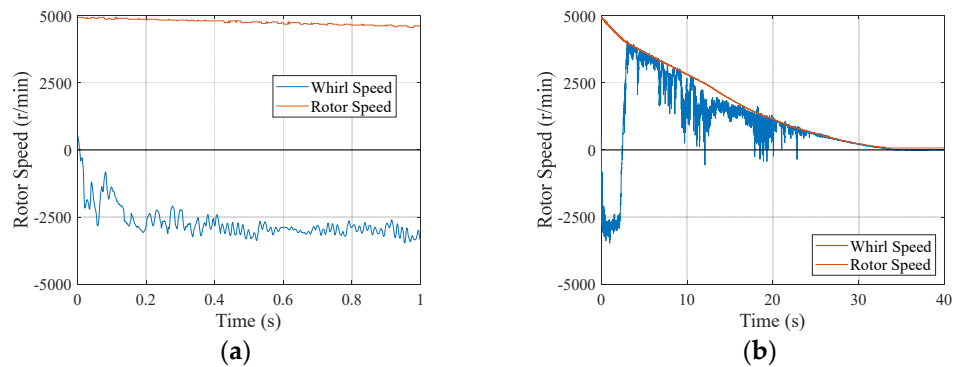


Figure 12. Rotor speed and whirl speed measured in the 5000 r/min drop test: (a) First second, (b) Whole process.

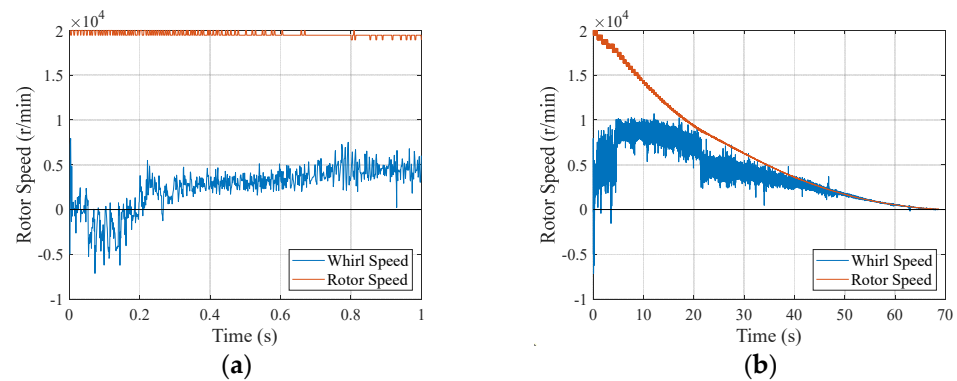


Figure 13. Rotor speed and whirl speed measured in the 20,000 r/min drop test: (a) First second, (b) Whole process.

At a 5000 r/min drop in Figure 12, the rotor quickly entered a full-rub whirl state. Compared to the simulation results, the rotor experienced a longer period of backward whirl and entered a forward dry-friction whirl state, then decelerated to zero velocity synchronously as in the simulation. At a 20,000 r/min drop in Figure 13, the rotor moved more quickly from the backward whirl into the forward whirl than at the 5000 r/min drop. Then, the rotor remained at a whirl speed of 6174 r/min, resulting in a dry-friction whip state. After the speed was greatly reduced, the whirl speed also gradually decreased synchronously with the rotor, changing from dry-friction whip to dry-friction whirl. The maximum temperature of the rolling body measured by the thermal imaging camera was 1.5 °C at 5000 r/min and 9.5 °C at 20,000 r/min above the ambient temperature, which were slightly lower than the simulation results, 2.4 °C at 5000 r/min and 10.5 °C at 20,000 r/min.

Based on a comparison of the simulation and experimental results from Figures 7, 9 and 11–13, the results are in good agreement, especially the occurrence of each state in the whole rotor drop process, which was accurately predicted. In addition, comparing the deceleration of the rotor in Figure 14 proved the computational validity of the simulation model throughout the whole drop process, indicating that the simulation model could accurately evaluate the process of drop energy conversion, which basically met the research needs to study the contact force and heat generation.

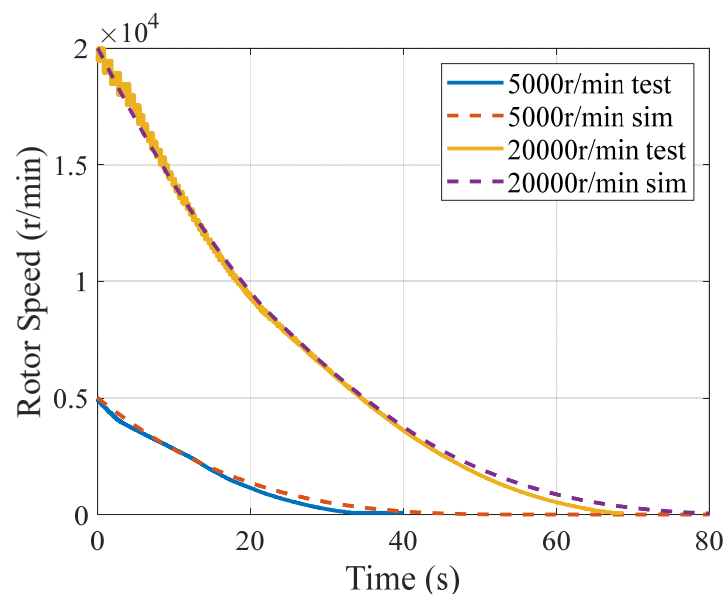


Figure 14. Comparison of rotor speed changes between simulation and experiment.

5. Conclusions

When a vertical rotor drops on the TDB, after several bounces in the axial direction, the rotor obtains a stable support. The friction of the contact surface drives the TDB inner ring to accelerate to the same rotational speed as the rotor. In the radial direction, the rotor enters whirl motion after the initial collisions. The whirl direction depends on the direction of friction, so the system first enters the backward whirl state and then stabilizes in the forward whirl state. There is a natural whirl frequency (rotational speed) and a critical speed, so the drop forward whirl is divided into the dry-friction whirl and whip states; the former occurs at low speeds, and the latter occurs at high speeds.

The dry-friction whip has a higher TDB contact force and temperature rise than the dry-friction whirl, which is due to the rotor speed and friction state. The contact force at the beginning of the drop increases with the drop speed. The contact force of the dry-friction whirl also increases with the drop speed, and the contact force of the dry-friction whip is not affected by the drop speed. Nonetheless, the significant temperature rise caused by sliding friction in dry-friction whip exposes the TDB to potential wear failure.

The above conclusions are drawn through the simulation of the dynamic and thermal coupled model. Compared with models in other studies, this model can simulate the whole process of drop and deceleration. A five-degree-of-freedom AMB-rotor-TDB system experimental bench was established, and a series of drop tests were performed. The drop speed was set to 5000 r/min and 20,000 r/min, and the results showed that the model and the experiment were in good agreement when considering the drop trajectory, rotation speed, and temperature rise, especially for the simulation of the rotor deceleration process, which had good repeatability.

Author Contributions: Methodology, writing—original draft preparation, Z.L.; conceptualization, M.L.; data curation, validation, G.Y.; software, J.Z.; resources, supervision, Y.W.; project administration, writing—review and editing, Z.W.; All authors have read and agreed to the published version of the manuscript.

Funding: This research was funded by the National Key R&D Program of China, grant No. 2018YFB2 000102 and the National Natural Science Foundation of China, grant No.52005467.

Conflicts of Interest: The authors declare no conflict of interest.

Nomenclature

a	contact ellipse long semiaxis
d_b, d_i, d_o	diameter of ball, inner ring, outer ring
d_m	$= (d_b + d_i)/2$
E	modulus of elasticity
f_0	surface friction media parameter
$F_{a,z}, F_a, P_a,$	contact force, frictional force, pressure on the axial end surface
F_r, F_t	radial impact force and tangential frictional force between rotor and TDB inner ring
$h_{b,a}, h_{b,r}$	axial and radial clearance of rotor and TDB
H	heat generation
k	conduction thermal conductivity coefficient
K	contact stiffness
$L(k)$	the second kind of completely elliptic integrals
m_r, J_r, e	rotor mass, inertia, and unbalance
M_a	friction torque on the axial end surface
M_b	friction torque of TDB
r	radius of curvature in the Hertz model
R	thermal resistance
R_1, R_2	inner and outer radius of TDB inner ring
T	temperature

v	Poisson's ratio
$v_{A,rb}, r, \varphi$	relative sliding velocity, radius, and phase angle at point A
z	number of balls
β	the nonlinear exponent determined from material and geometric properties of the local region of the contacting bodies
λ	contact coefficient of Hunt-Crossley model, valued 0.08–0.32 s/m
θ_b, θ_r	rotational angle of TDB inner ring and rotor
μ_a, μ_r	axial and radial friction coefficient between rotor and TDB inner ring
ρ, α	polar coordinate representation of rotor center
Subscripts	
a	axial direction
b	ball
h	housing
i	Inner race
o	outer race
r	radial direction
s	rotor

References

- Schweitzer, G. Safety and Reliability Aspects for Active Magnetic Bearing Applications—A Survey. *Proc. Inst. Mech. Eng. Part I J. Syst. Control Eng.* **2005**, *219*, 383–392. [\[CrossRef\]](#)
- ISO 14839-4; Mechanical Vibration—Vibration of Rotating Machinery Equipped with Active Magnetic Bearings Part 4: Technical Guidelines. International Organization for Standardization: Geneva, Switzerland, 2012.
- Lyu, M.; Liu, T.; Wang, Z.; Yan, S.; Jia, X.; Wang, Y. Orbit Response Recognition during Touchdowns by Instantaneous Frequency in Active Magnetic Bearings. *J. Vib. Acoust. Trans. ASME* **2018**, *140*, 1–11. [\[CrossRef\]](#)
- Lyu, M.; Wang, Z.; Liu, T.; Jia, X.; Wang, Y. Frequency Analysis of the Orbit Responses of Active Magnetic Bearings in Touchdown Using Hilbert Transform. *Int. J. Struct. Stab. Dyn.* **2017**, *17*, 17500869. [\[CrossRef\]](#)
- Lyu, M.; Liu, T.; Wang, Z.; Yan, S.; Jia, X.; Wang, Y. A Control Method of the Rotor Re-Levitation for Different Orbit Responses during Touchdowns in Active Magnetic Bearings. *Mech. Syst. Signal Process.* **2018**, *105*, 241–260. [\[CrossRef\]](#)
- Kang, X.; Palazzolo, A.; Zhong, W. Auxiliary Bearing Squeeze Film Dampers for Magnetic Bearing Supported Rotors. *Tribol. Int.* **2020**, *146*, 106181. [\[CrossRef\]](#)
- Ishii, T.; Kirk, R.G. Transient Response Technique Applied to Active Magnetic Bearing Machinery during Rotor Drop. *ASME J. Vib. Acoust.* **1996**, *118*, 154–163. [\[CrossRef\]](#)
- Kärkkäinen, A.; Söponen, J.; Mikkola, A. Dynamic Simulation of a Flexible Rotor during Drop on Retainer Bearings. *J. Sound Vib.* **2007**, *306*, 601–617. [\[CrossRef\]](#)
- Hunt, K.; Crossley, E. Coefficient of Restitution Interpreted as Damping in Vibroimpact to Cite This Version: HAL Id: Hal-01333795 Coefficient of Restitution Interpreted as Damping in Vibroimpact. *J. Appl. Mech. Am. Soc. Mech. Eng.* **1975**, *42*, 440–445. [\[CrossRef\]](#)
- Jarroux, C.; Dufour, R.; Mahfoud, J.; Defoy, B.; Alban, T.; Delgado, A. Touchdown Bearing Models for Rotor-AMB Systems. *J. Sound Vib.* **2019**, *440*, 51–69. [\[CrossRef\]](#)
- Neisi, N.; Sikanen, E.; Heikkinen, J.E.; Söponen, J. Stress Analysis of a Touchdown Bearing Having an Artificial Crack. *Proc. ASME Des. Eng. Tech. Conf.* **2017**, *8*, 1–9. [\[CrossRef\]](#)
- Fonseca, C.A.; Santos, I.F.; Weber, H.I. Influence of Unbalance Levels on Nonlinear Dynamics of a Rotor-Backup Rolling Bearing System. *J. Sound Vib.* **2017**, *394*, 482–496. [\[CrossRef\]](#)
- Halminen, O.; Kärkkäinen, A.; Söponen, J.; Mikkola, A. Active Magnetic Bearing-Supported Rotor with Misaligned Cageless Backup Bearings: A Dropdown Event Simulation Model. *Mech. Syst. Signal Process.* **2015**, *50–51*, 692–705. [\[CrossRef\]](#)
- Gupta, P.K.; Taketa, J.I.; Price, C.M. Thermal Interactions in Rolling Bearings. *Proc. Inst. Mech. Eng. Part J J. Eng. Tribol.* **2020**, *234*, 1233–1253. [\[CrossRef\]](#)
- Sun, G. Auxiliary Bearing Life Prediction Using Hertzian Contact Bearing Model. *J. Vib. Acoust.* **2006**, *128*, 203. [\[CrossRef\]](#)
- Caprio, M.T.; Murphy, B.T.; Herbst, J.D. Spin Commissioning and Drop Tests of a 130 KW-Hr Composite Flywheel. In Proceedings of the 9th International Symposium on Magnetic Bearings, Lexington, KY, USA, 3–6 August 2004.
- Reid, C.M.; Miller, T.B.; Hoberecht, M.A.; Loyselle, P.L.; Taylor, L.M.; Farmer, S.C.; Jansen, R.H. History of Electrochemical and Energy Storage Technology Development at NASA Glenn Research Center. *J. Aerosp. Eng.* **2013**, *26*, 361–371. [\[CrossRef\]](#)
- Hawkins, L.; McMullen, P.; Vuong, V. Development and Testing of the Backup Bearing System for an AMB Energy Storage Flywheel. In Proceedings of the Turbo Expo: Power for Land, Sea, and Air, ASMEDC, Montreal, QC, Canada, 14–17 May 2007; pp. 1055–1062.
- Zhao, Y.; Yang, G.; Shi, Z.; Zhao, L. Thermal Analysis and Simulation of Auxiliary Bearings and Its Application in the High Temperature Reactor-10. *J. Tribol.* **2016**, *138*, 011102. [\[CrossRef\]](#)
- Wilkes, J.C.; Childs, D.W.; Dyck, B.J.; Phillips, S.G. The Numerical and Experimental Characteristics of Multimode Dry-Friction Whip and Whirl. *J. Eng. Gas Turbines Power* **2010**, *132*, 052503. [\[CrossRef\]](#)

21. Wilkes, J.; Moore, J.; Ransom, D.; Vannini, G. An Improved Catcher Bearing Model and an Explanation of the Forward Whirl/Whip Phenomenon Observed in Active Magnetic Bearing Transient Drop Experiments. *J. Eng. Gas Turbines Power* **2014**, *136*, 1–11. [[CrossRef](#)]
22. Jacobs, D.A.; Waldron, K.J. Modeling Inelastic Collisions with the Hunt-Crossley Model Using the Energetic Coefficient of Restitution. *J. Comput. Nonlinear Dyn.* **2015**, *10*, 021001. [[CrossRef](#)]
23. Halminen, O.; Aceituno, J.F.; Escalona, J.L.; Sopanen, J.; Mikkola, A. Models for Dynamic Analysis of Backup Ball Bearings of an AMB-System. *Mech. Syst. Signal Process.* **2017**, *95*, 324–344. [[CrossRef](#)]
24. Takabi, J.; Khonsari, M.M. On the Thermally-Induced Failure of Rolling Element Bearings. *Tribol. Int.* **2015**, *94*, 661–674. [[CrossRef](#)]